Journal of Alloys and Compounds 509 (2011) 66–71

Contents lists available at ScienceDirect

Journal of Alloys and Compounds

journal homepage: www.elsevier.com/locate/jallcom

Synthesis, structure, and high temperature Mössbauer and Raman spectroscopy studies of $Ba_{1.6}Sr_{1.4}Fe_2WO_9$ double perovskite

B. Manoun[a,c,*], S. Benmokhtar[b], L. Bih[a], M. Azrour[a], A. Ezzahi[c], A. Ider[c], M. Azdouz[a], H. Annersten[d], P. Lazor[d]

[a] Laboratoire de Physico-Chimie des Matériaux, Département de Chimie, FST Errachidia, Morocco
[b] Laboratoire de chimie des Matériaux Solides (LCMS), Département de Chimie, Faculté des Sciences Ben M'Sik Casablanca, Morocco
[c] Equipe Matériaux et environnement, laboratoire des Procédés de Valorisation des Ressources Naturelles, des Matériaux et Environnement, FST Settat, Morocco
[d] Department of Earth Sciences, Uppsala University, S-752 36 Uppsala, Morocco

ARTICLE INFO

Article history:
Received 26 April 2010
Received in revised form 18 August 2010
Accepted 24 August 2010
Available online 29 September 2010

Keywords:
Double perovskite
High temperature
Rietveld
X-ray diffraction
Mössbauer spectroscopy
Raman spectroscopy
$Ba_{1.6}Sr_{1.4}Fe_2WO_9$

ABSTRACT

$Ba_{1.6}Sr_{1.4}Fe_2WO_9$ has been prepared in polycrystalline form by solid-state reaction method in air, and has been studied by X-ray powder diffraction method (XRPD), and high temperature Mössbauer and Raman spectroscopies. The crystal structure was resolved at room temperature by the Rietveld refinement method, and revealed that $Ba_{1.6}Sr_{1.4}Fe_2WO_9$ crystallizes in a tetragonal system, space group I4/m, with $a = b = 5.6489(10)$Å, $c = 7.9833(2)$Å and adopts a double perovskite-type $A_3B'_2B''O_9$ (A = Ba, Sr; B′ = Fe/W, and B″ = Fe/W) structure described by the crystallographic formula $(Ba_{1.07}Sr_{0.93})_{4d}(Fe_{0.744}W_{0.256})_{2a}(Fe_{0.585}W_{0.415})_{2b}O_6$. The structure contains alternating $[(Fe/W)_{2a}O_6]$ and $[(Fe/W)_{2b}O_6]$ octahedra. Mössbauer studies reveal the presence of iron in the 3+ oxidation state. The high temperature Mössbauer measurements showed a magnetic to paramagnetic transition around 405 ± 10 K. The transition is gradual over the temperature interval. The decrease in isomer shift is in line with the general temperature dependence. While the isomer shift is rather linear over the whole temperature range, the quadratic dipolar ΔE temperature dependence shows an abrupt change at 405 K. The latter results allow concluding that a temperature-induced phase transition had occurred. The high temperature Raman study confirms the Mössbauer results on the magnetic to paramagnetic transition.

1. Introduction

Double perovskite materials of general formula $A_2BB'O_6$ (where A is an alkaline-earth or rare-earth ion, B and B′ are different transition metal cations) represent a wide field of investigation which appears promising for various applications [1]. A_2FeMoO_6 (A = Sr, Ba) [2–4] and many of its structural materials [5,6], have attracted considerable scientific and technological interest in recent years due to its reported room temperature (415 °C for Sr_2FeMoO_6 and 330 °C for Ba_2FeMoO_6) low-field magneto-resistance [7,8]. This property, related to the variation of electric resistivity when a magnetic field is applied, is a consequence of the half-metallic character of the double perovskite, and can also been attributed to spin dependent scattering of charge carriers at grain boundaries extended to inter grain-tunneling effect. Recently considerable studies have been done on different double perovskite series: Liu et al. reported on the structural transition and atomic ordering of a new series of ordered double perovskite oxides $Sr_2Fe_xMo_{2-x}O_6$ ($0.8 \le x \le 1.5$) [9]; the XRD studies indicates that the crystal structure of the compounds $Sr_2Fe_xMo_{2-x}O_6$ changes from a tetragonal I4/mmm lattice to a cubic Fm-3m lattice around $x = 1.2$; the crystal structure results showed that the degree of ordering in $Sr_2Fe_xMo_{2-x}O_6$ exhibits a maximal at $x = 0.95$. El-Hagary investigated the system $Ba_2Fe_{1-x}Cr_xMoO_6$ with ($0 \le x \le 1$) [10], to see the effect of partial substitution of Cr^{3+} for Fe^{3+} on magnetism, magnetocaloric effect and transport properties of Ba_2FeMoO_6 double perovskites and they conclude that this perovskite is beneficial for the household application of active magnetic refrigerant materials. The zero field electrical resistivity measurements exhibit a change from metallic behavior at $x = 0$ to semiconducting like behavior for all doped samples ($x \ge 0.2$) over the entire measurement temperature region from 4.2 to 300 K. Hankare et al. reported in a recent study on the synthesis, characterization and electrical properties of the system $LaMn_xFe_{1-x}O_3$ [11]. The electrical properties of the compounds show that, they exhibit semiconducting behavior. The substitution of manganese ions plays an important role in changing their structural, electrical and magnetic properties of lanthanum ferrite. There are various reports on the effect of substitutions of cations at 'A' site with different ionic radii. The variation of 'A' site

* Corresponding author at: Faculté Polydisciplinaire Khouribgha, Université Hassan 1er, Bp 145, Morocco.
E-mail address: manounb@gmail.com (B. Manoun).

0925-8388/$ – see front matter © 2010 Elsevier B.V. All rights reserved.
doi:10.1016/j.jallcom.2010.08.082

Table 1
Positional and thermal parameters for $Ba_{1.6}Sr_{1.4}Fe_2WO_9$ after a Rietveld refinement XRPD data collected at 298 K; space group: I4/m, $Z=2$. Unit-cell parameters: $a=b=5.6490(3)$Å, $c=7.9832(2)$Å, $V=254.75(6)$Å^3.

Atom	Wyckoff site	x	y	z	Biso/Å^2	Occ
Ba/Sr	4d	0.0	1/2	1/4	0.65	0.532(5)/0.467(5)
Fe(1)/W(1)	2a	0.0	0.0	0.0	0.35	0.744(1)/0.256(1)
W(2)/Fe(2)	2b	0.0	0.0	1/2	0.35	0.415(2)/0.585(2)
O(1)	8h	0.2702(3)	0.2300(2)	0.0	2.30	1
O(2)	4e	0.0	0.0	0.2615(2)	2.30	1

Reliability factors for the XRPD data: $R_{Bragg}=4.0\%$, $R_P=3.66\%$, $R_{WP}=4.77\%$, $R_{exp}=4.09\%$, $\chi^2=1.36$.

cation will lead to changes in the properties of the system including ferromagnetic transition temperature and magnetic ordering which is having a direct impact on the ultimate magneto-resistive properties of the system [12,13]. The change in the properties are caused by the change in chemical pressure brought about by the substitution of cations differing in ionic radii, which in turn affect the extent of orbital overlap and exchange coupling strength through the change in bond length and bond angle of Fe–O–W. Also the substitution at 'A' site has a direct impact on antisite disorder defects. These antisite disorder defects affect half-metallic nature, ferromagnetic transition temperature, saturation magnetic moment value and also low-field magneto-resistance value [14,15]. For an exact estimation of various properties of these double perovskite systems, the contribution of antisite disorder defects cannot be ignored.

In this study, we report on the effect of Sr substitution at A-site in the polycrystalline system $Ba_{3-x}Sr_xFe_2WO_9$ (with $x=1.4$). The double perovskite oxide $Ba_{1.6}Sr_{1.4}Fe_2WO_9$ was prepared by solid-state method, and its crystal structure was solved by Rietveld refinements of X-ray powders diffraction patterns, ^{57}Fe Mössbauer spectroscopy provides information about the electronic configuration of iron and its crystallographic environment. The study with high temperature Raman spectroscopy showed the phase transition from the tetragonal to the cubic system which confirms the data observed by Mössbauer spectroscopy.

2. Experimental

2.1. Synthesis

Polycrystalline powder of $Ba_{1.6}Sr_{1.4}Fe_2WO_9$ was synthesized in alumina crucible using the standard solid-state reaction from stoichiometric mixtures of $BaCO_3$ (99.99%), $SrCO_3$ (99.997%), Fe_2O_3 (99.8%) and WO_3 (99.99%) Alfa Aesar. The mixture was ground in an agate mortar then heated progressively to 650 and 900 °C for 18 h. The resulting powder was reground and calcined at 1100 °C for 24 h in air.

2.2. Instrumental methods

2.2.1. X-ray diffraction

The purity of this phase was controlled by X-ray powder diffraction (XRPD) patterns obtained with a Bruker D8 diffractometer (40 kV, 50 mA, Cu Kα_1 = 1.54059 Å radiation). The XRPD data for Rietveld analysis were collected with the same diffractometer equipped with a Ge 111 incident beam monochromator and a Braun linear position sensitive detector. Scans were recorded over a 2θ range of 15–120°. A step size of 0.02° 2θ was used, and the counting time was 30 s/step. Structure refinements were carried out using the Rietveld method with the Fullprof software [16]. A polynomial function with six parameters was used to fit the background. The profiles have been fitted using a Pseudo-Voigt function.

2.2.2. Mössbauer spectroscopy

Powder transmission ^{57}Fe Mössbauer spectra were obtained on powder samples mounted on a thin Al-foil in a Pt-wired furnace regulated between 293 and 600 K. Temperature was regulated from a thermocouple inserted in the copper holder of the sample plate. Temperatures given are within ±5 K. Mössbauer source used was ^{57}Co in Rh with a nominal strength of 50 mCi at room temperature in conjugation with 512 MCA and saw tooth shape acceleration mode of the vibrator. The mirror symmetric spectra, 256 channels each, were folded and computer fitted using a least square fitting program developed by Jernberg and Sundqvist [17]. Velocity calibration of spectra was performed against α-iron.

2.2.3. Raman spectroscopy

The Raman spectra were recorded with an imaging spectrometer (HoloSpec f/1.8i, Kaiser Optical Systems) equipped with a holographic transmission grating and thermoelectrically cooled two-dimensional multichannel CCD detector (Newton, Andor Technology, 1600 × 400 pixels, −60 °C). An argon laser was used for the excitation: the 514.5 nm wavelength radiation was chosen. The spectrometer was calibrated by fluorescence lines of the neon lamp. Non-polarized Raman spectra were collected in the back-scattering geometry, in the range 180–2280 cm^{-1}, at a resolution of about 3 cm^{-1}. Accuracy of spectral measurements, resulting from the wavelength calibration procedure and experimental conditions, is estimated to be about 1.5 cm^{-1}. Precision of the reported peak positions, as represented by standard errors obtained in peak fits, varied between 0.04 and 0.7 cm^{-1}, the lower values representative for singlets and low temperatures, the higher values characteristic for overlapping peaks and high temperatures. The acquisition time varied from 30 s to 5 min.

Heating was accomplished using a mica insulated band heater (DuraBand, 200 W, Tempco Electric Heater Corporation) mounted around the sample ceramic holder and connected to a variable transformer. Temperature changes during the heating/cooling cycles were induced and controlled by adjusting the transformer's voltage (0–240 V) and monitored with an accuracy of ±1 K by the K-type thermocouple adjacent to the sample. Temperatures were stabilized to within 1 and 3 °C, for the low (25 °C) and high (350 °C) temperature measurements, respectively.

3. Results and discussion

3.1. Structural determination

The experimental powder diffraction pattern was indexed by DICVOL04 software [18]. The observed reflection conditions $h\,k\,l$, $h+k+l=2n$; $h\,k\,0$, $h+k=2n$; $0\,k\,l$, $k+l=2n$; $h\,h\,l$, $l=2n$; $0\,0\,l$, $l=2n$; and $h\,0\,0$, $h=2n$ lead to the space group I4/m (tetragonal system) with $a=b=5.6477(2)$, $c=7.9874(3)$Å and $V=254.77(8)$Å^3 with the following figures of merits F9 = 48.2(0.0081,23) and M9 = 229.7. The unit-cell parameters are related to a_0 (ideal cubic perovskite, $a_0=3.89$ Å) as $a\approx b\approx\sqrt{2}a_0$ and $c\approx 2a_0$. The unit-cell parameters and the space group were confirmed with the Rietveld refinements using the FULLPROF program [16]. The final reliability factors obtained in the last refinement are $R_P=0.037$; $R_{WP}=0.048$; $R_{exp}=0.041$; $R_B=0.04$, $\chi^2=1.36$. There is a similarity between the parameters of $Ba_{1.6}Sr_{1.4}Fe_2WO_9$ and those of $Sr_3Fe_2MO_9$ perovskite which crystallize in the tetragonal system (space group: I4/m) at ambient temperature (M = W: $a=b=5.5784(2)$Å, $c=7.8659(2)$Å; M = Mo: $a=b=5.5608(2)$Å, $c=7.8471(4)$Å; M = Te: $a=b=5.5614(7)$Å, $c=7.867(1)$Å) [19–21]. The high values observed for the studied compound are due to the size of Ba (1.36 Å) greater than that of Sr (1.18 Å) [22].

3.2. Rietveld refinement

The crystal structure of $Ba_{1.6}Sr_{1.4}Fe_2WO_9$ was refined by the Rietveld method [23], using the FULLPROF program [16]. The refinement was undertaken in the tetragonal structure, space group I4/m (No. 87, Glazer's notation $a^0a^0c^-$), Ba and Sr atoms were located at the 4d (0,1/2,1/4) positions, the Fe and W atoms were allowed to occupy the two possible positions of sites Fe/W at 2a (0,0,0) and Fe/W at 2b (0,0,1/2) sites, and oxygen atoms at the 4e (0,0,z) and 8 h (x,y,0) positions. The possibility of Fe/W antisite disordering, assuming that some W from the 2b positions could randomly

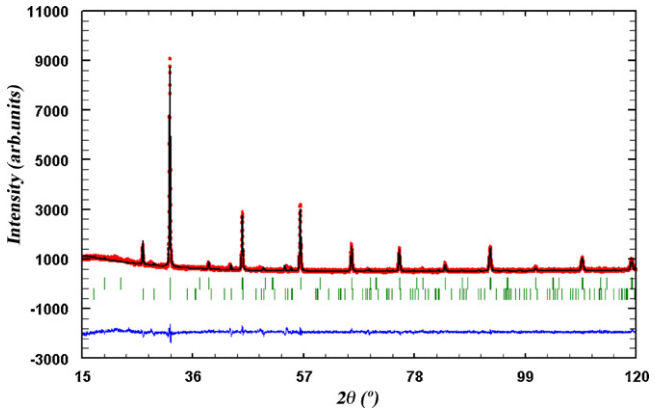

Fig. 1. The observed, calculated, and difference plots for the fit patterns of $Ba_{1.6}Sr_{1.4}Fe_2WO_9$ after Rietveld refinement. The (Ba/Sr)WO_4 impurity was included in the refinements.

Table 2
Some selected bond distances and angles for $Ba_{1.6}Sr_{1.4}Fe_2WO_9$ at 298 K.

$(Ba/Sr)O_{12}$ icosahedron	Distances (Å)
(Ba/Sr)–O(1) (×4)	2.939(4)
(Ba/Sr)–O(1) (×4)	2.712(4)
(Ba/Sr)–O(2) (×4)	2.826(5)
⟨Ba/Sr–O⟩	2.826(2)
$(Fe/W)_{2a}O_6$ octahedron	
$(Fe/W)_{2a}$–O(1) (×4)	2.004(3)
$(Fe/W)_{2a}$–O(2) (×2)	2.088(5)
⟨$(Fe/W)_{2a}$–O⟩	2.046(2)
$(Fe/W)_{2b}O_6$ octahedron	
$(Fe/W)_{2b}$–O(1) (×4)	2.003(3)
$(Fe/W)_{2b}$–O(2) (×2)	1.904(5)
⟨$(Fe/W)_{2b}$–O⟩	1.953(4)
Angles	
$(Fe/W)_{2a}$–O(1)–(Fe/W)2b	170.82(3)
$(Fe/W)_{2a}$–O(2)–(Fe/W)2b	180.00

replace some Fe at 2a positions was also checked. A major Fe occupancy (74.5%) is observed at 2a positions, whereas 2b sites are approximately half occupied by Fe (58.5%) and W (41.5%). The thermal factors for 2a and 2b positions were constrained. The good agreement between observed and calculated XRPD profiles is illustrated in Fig. 1. Table 1 includes the final atomic coordinates and discrepancy factors after the refinement. Table 2 lists the main interatomic distances and angles. Note that the (Ba/Sr)WO_4 impurity was included in the refinements.

3.3. Description of the structure

The structure of $Ba_{1.6}Sr_{1.4}Fe_2WO_9$ consists of a three-dimensional (3D) framework built up from alternating $[(Fe/W)_{2a}O_6]$ and $[(Fe/W)_{2b}O_6]$ octahedra (Fig. 2), the crystallographic formula can be written as $(Ba_{1.07}Sr_{0.93})_{4d}(Fe_{0.744}W_{0.256})_{2a}(Fe_{0.585}W_{0.415})_{2b}O_6$. The bond lengths between the cations and oxygen are shown in Table 2, these values reveal very slight distortions of the $[(Fe/W)_{2a}O_6]$ and $[(Fe/W)_{2b}O_6]$ octahedra. The distances between $(Fe/W)_{2a}$ and O in the $(a-b)$ plane and parallel to the c-axis were 2.004(3) and 2.088(5)Å, respectively. The distances between $(Fe/W)_{2b}$ and O in the $(a-b)$ plane and parallel to the c-axis were about 2.003(3) and 1.904(5)Å, respectively. The volumes of the $[(Fe/W)_{2a}O_6]$ and $[(Fe/W)_{2b}O_6]$ octahedra were calculated to be 11.427(4) and 9.949(5)$Å^3$, respectively. The $[(Fe/W)_{2a}O_6]$ and $[(Fe/W)_{2b}O_6]$ octahedra are ordered and alternate along the three directions in the crystal structure

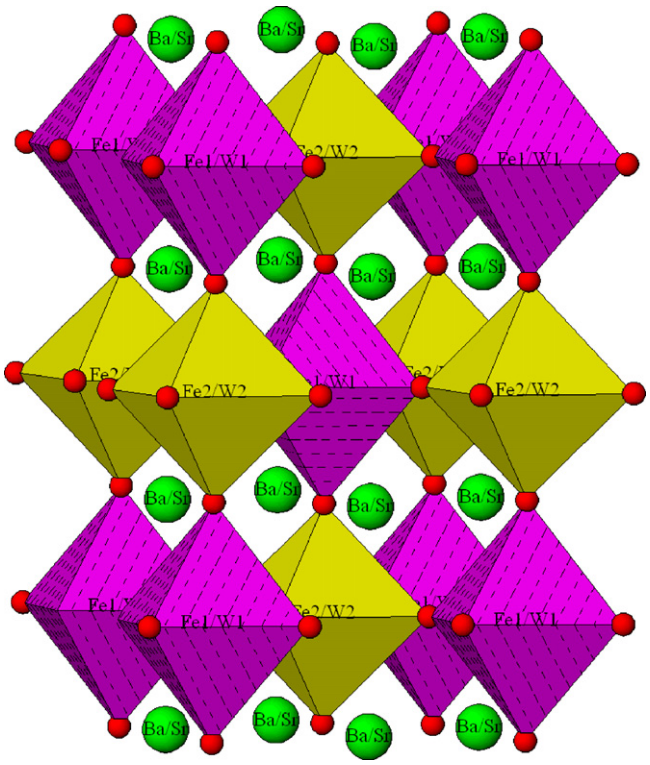

Fig. 2. Polyhedral view of the crystal structure of $Ba_{1.6}Sr_{1.4}Fe_2WO_9$. *Large spheres* represent the Ba/Sr cations. Fe and W cations are located inside the *octahedra*.

in such a way that each $[(Fe/W)_{2a}O_6]$ octahedron is linked, via corners, to six $[(Fe/W)_{2b}O_6]$ octahedra and vice versa (Fig. 2). Fig. 3 shows the $(a^0a^0c^-)$-tilt, which means, in the usual Glazer's notation [24,25], that successive octahedra along [0 0 1] axis have opposite signs of the tilts, and that there is no tilt along [1 0 0] and [0 1 0].

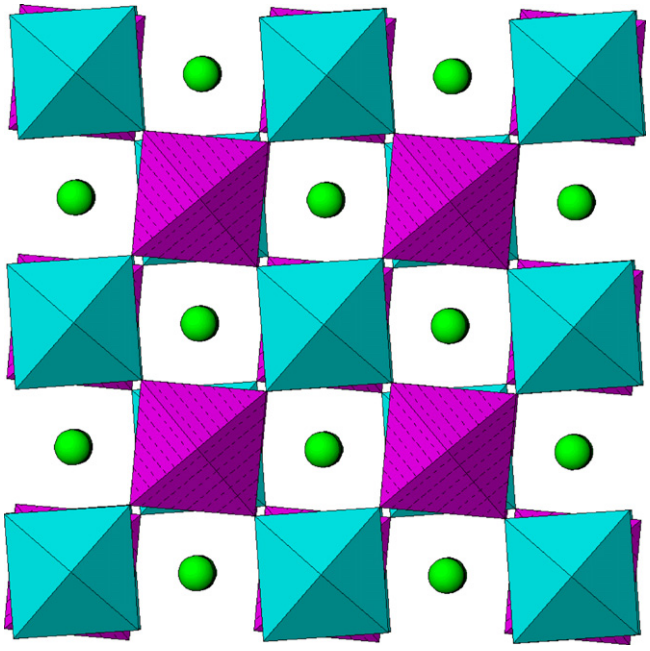

Fig. 3. $(a^0b^0c^-)$ octahedral-tilt around vertical [0 0 1] axis in $Ba_{1.6}Sr_{1.4}Fe_2WO_9$ perovskite.

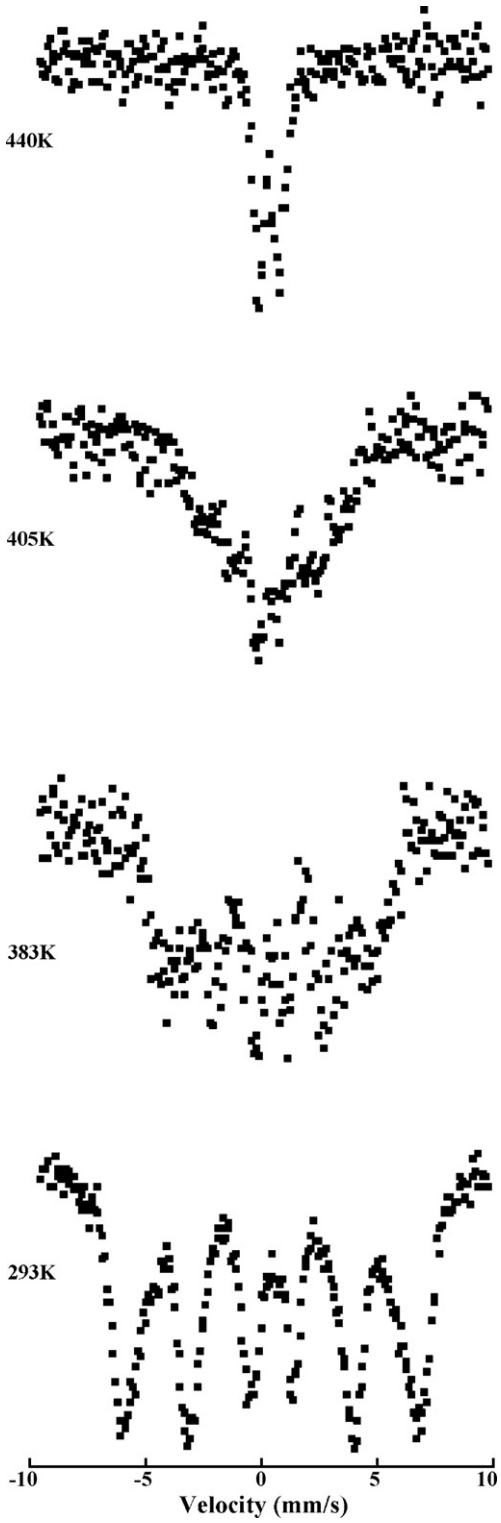

Fig. 4. Mössbauer spectra of $Ba_{1.6}Sr_{1.4}Fe_2WO_9$ showing gradual magnetic ordering.

3.4. Mössbauer spectroscopy

The ^{57}Fe Mössbauer spectra recorded in situ for $Ba_{1.6}Sr_{1.4}Fe_2WO_9$ in the temperature range 293–573 K are shown in Fig. 4. A ferromagnetic to paramagnetic transition is observed at temperature below 405 K (Fig. 5). The transition was gradual ≈20 K suggesting a temperature dependent ordering of the magnetic spins most probably due to local disorder in $Ba_{1.6}Sr_{1.4}Fe_2WO_9$. The

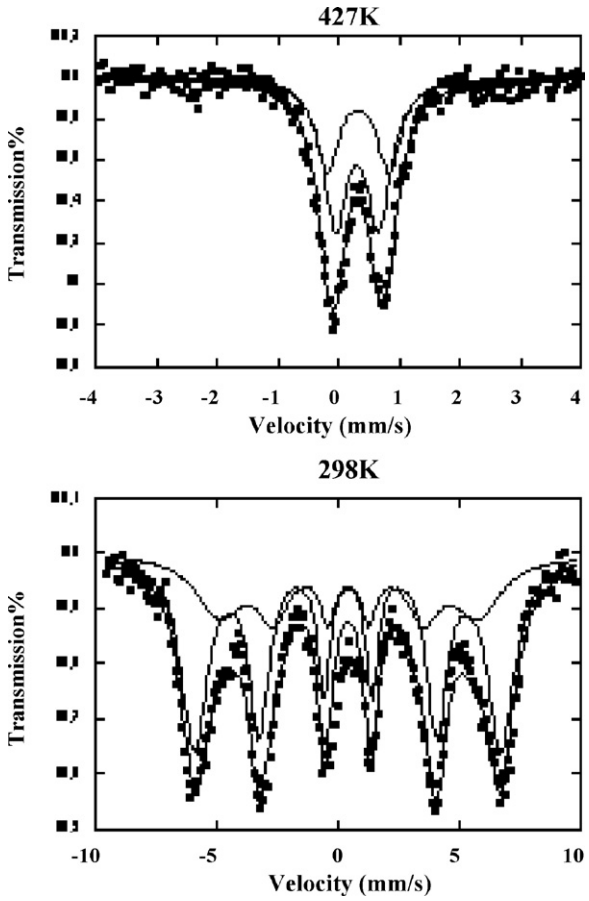

Fig. 5. Fitted paramagnetic Mössbauer spectra at 427 K above the magnetic ordering temperature (top) and below at room temperature (bottom).

resonant spectra above and below the transition could be resolved in two doublets and two sextets by computer fitting the raw spectra (Fig. 4). The obtained Mössbauer parameters are given in Table 3. According to Menil [26], the usual ranges of isomer shifts in iron oxides are 0.29–0.50 mm/s and typical for Fe^{3+} in 6-coordination. The Δ-value drops drastically at the magnetic transition and is not an evidence for a major crystallographic structure. Below the magnetic ordering temperature a combined magnetic and quadrupole interaction lowers the quadrupole shift. Although there is a close overlap of the sub-spectra two different types of octahedral sites are resolved in the double perovskite structure. Site occupancy (X^{Fe}) is calculated from the observed area ratios of the respective resonance lines and is within ±3%, the results are in fair agreement with those obtained from Rietveld refinement. Fe site (1) with isomer shift 0.33 mm/s at 427 K/0.42 mm/s at 293 K is the largest octahedral that have the highest X^{Fe} 0.78 at 427 K and 0.68 at 293 K in line with the larger mean cation radii 0.63 Å. This site thus belongs to the 2a crystallographic site. Mössbauer parameters Fe site (2) can therefore be assigned to the crystallographic site 2b also showing a pronounced cation disorder among the available octahedral sites. The larger quadrupole splitting of Fe in the site

Table 3
Mössbauer parameters for $Ba_{1.6}Sr_{1.4}Fe_2WO_9$ compound.

T (K)	δ (mm/s)	Δ (mm/s)	Area %	H_{eff} (T)	Fe occupancy
293	0.42	0.01	34.00	33.0	0.68
	0.39	0.01	65.00	39.0	0.65
427	0.33	1.02	39.0	0.0	0.78
	0.31	0.71	61.0	0.0	0.61

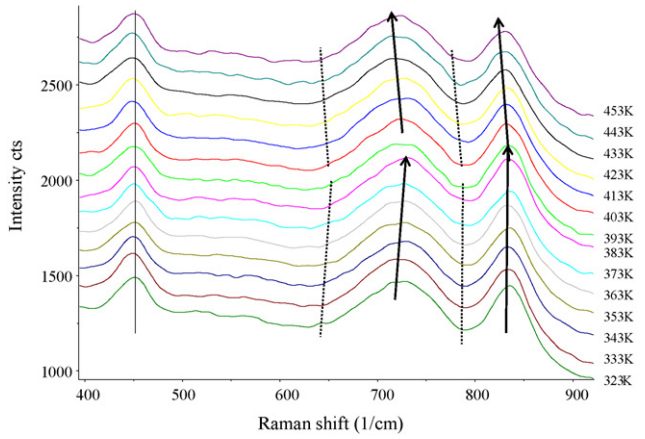

Fig. 6. Raman spectra of $Ba_{1.6}Sr_{1.4}Fe_2WO_9$ material obtained for selected temperatures, as indicated. A clear transition from tetragonal to cubic system is observed.

2a suggest a larger distortion compared to site 2b. The hyperfine field increased 5 T after heat treatment to 600 K and slow cooling down to room temperature suggesting an increased temperature dependent ordered ring magnetic spins.

3.5. High temperature Raman spectroscopy

Raman spectra of $Ba_{1.6}Sr_{1.4}Fe_2WO_9$ were collected in situ at room-pressure and elevated temperatures, up to 625 K. The Raman spectra obtained at several temperatures are presented in Fig. 6. The temperature dependence of the stretching modes is presented in Fig. 7.

The strongest temperature-induced changes in peak positions were observed for the modes recorded around 720 and 830 cm^{-1}. These modes exhibit monotonous shifts while temperature is increased up to 383 K, surprisingly toward higher wavenumbers.

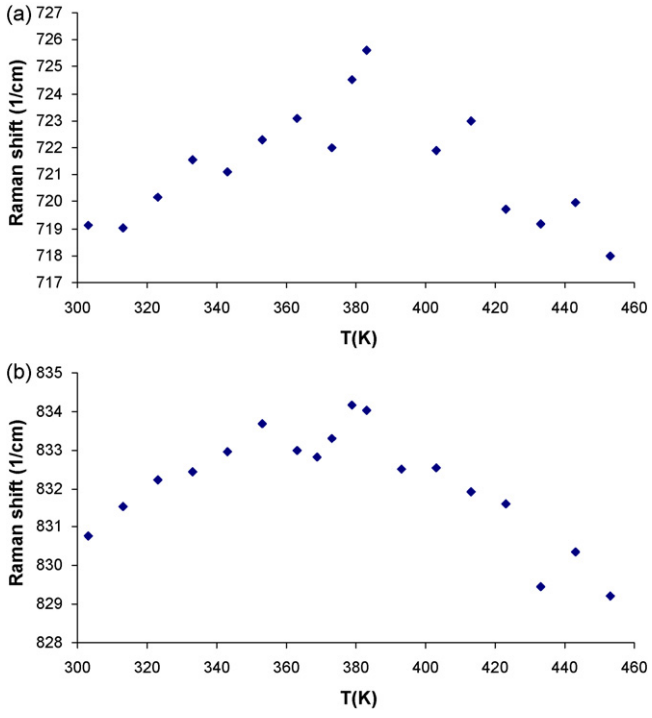

Fig. 7. Raman modes of $Ba_{1.6}Sr_{1.4}Fe_2WO_9$ vs. temperature, the transition from the tetragonal phase to the cubic phase shows considerable changes in temperature dependence of the modes centered at 720 cm^{-1} (a) and 830 cm^{-1} (b).

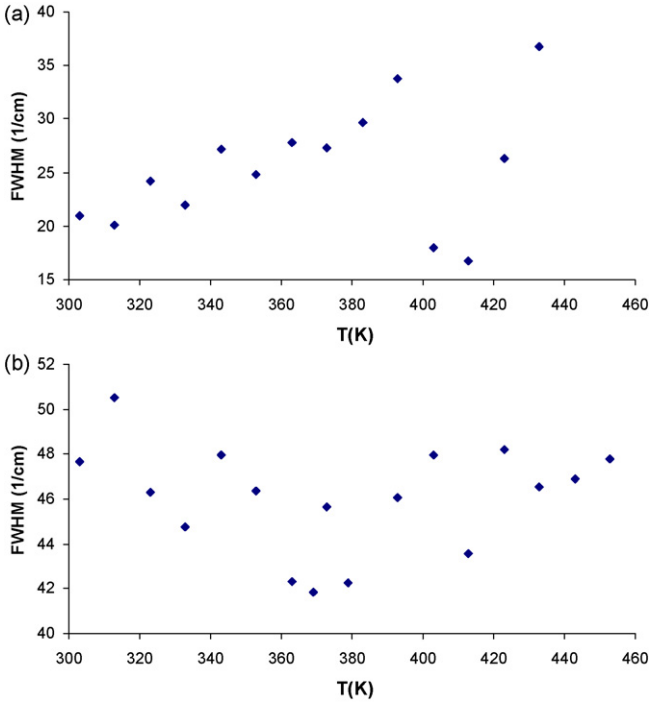

Fig. 8. FWHM of the 450 cm^{-1} (a) and 720 cm^{-1} (b) modes as a function of temperature, different behaviors are observed but both show the signs of the occurrence of the phase transition for the material.

Upon further temperature increase, considerable changes in the temperature dependence of the modes were observed, characterized by the reversal to a normal trend, toward lower wavenumbers. These changes are directly related to the phase transition from the tetragonal to the cubic phase which confirms the data observed by the Mössbauer spectroscopy.

The phase transition is evident from the plot of the temperature dependence of the FWHM (full width at half maximum) peak-profile parameter of the most intense mode, as shown in Fig. 8. This plot aids the investigation of the level of band broadening associated with the structural transition. The band shapes are described by the mode broadening parameters FWHM. By plotting these FWHMs as a function of temperature, a sensitive guide to the onset of the phase transition is obtained. For the 450 cm^{-1} mode, a large increase of FWHM with the increase in temperature is observed and clear transitional effects are observed (Fig. 8a): the widths behaving in a linear way as a function of temperature; when the temperature reached around 390 K, a drop in width of this mode is observed, thus signifying the occurrence of the transition. The mode 720 cm^{-1} exhibits a qualitatively different trend (Fig. 8b): the FWHM decreases as a function of temperature up to the transition point, followed by the FWHM increase beyond the transition. Also we plot in Fig. 9 the relative changes in intensities as a function of temperature; the phase transition is clearly recognized.

These results agree well with those of Mössbauer spectroscopy where the magnetic to paramagnetic transition was observed and probably changing the structure from tetragonal at low temperatures to cubic at high temperatures. The main difference between these two structures is the rotation of the BO_6 and $B'O_6$ octahedra around the tetragonal axis in the tetragonal phase. These distortions must occur due to the competing bonding preferences of the Ba/Sr and the two Fe/W site ions. At high temperatures both the expanded cell, and the greater thermal motion of the atoms, allow those to form a cubic cell, however, on cooling the increased bond strain drives the tetragonal distortion.

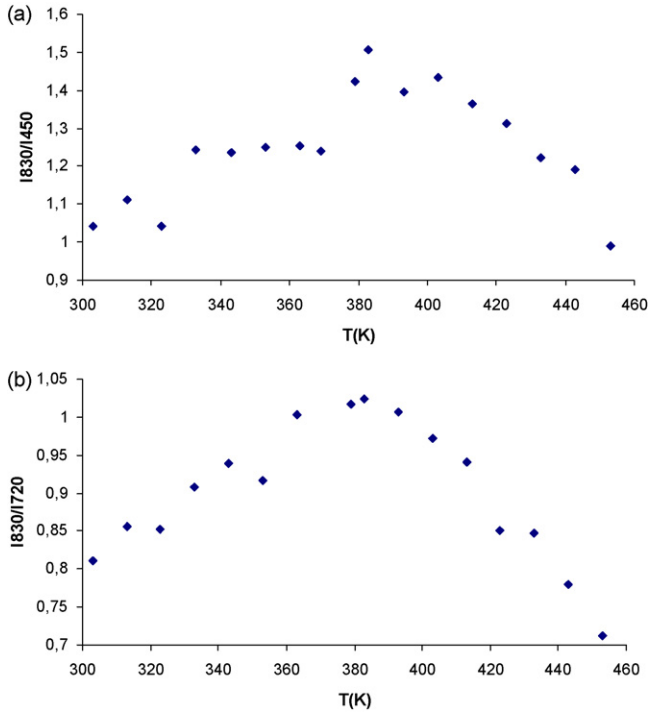

Fig. 9. Intensity ratio changes ($I830/I450$) (a) and ($I830/I720$) (b) as a function of temperature, the transition is observed above 380 K.

4. Conclusions

The tungsten oxide $Ba_{1.6}Sr_{1.4}Fe_2WO_9$ has been synthesized via solid-state reaction process, and characterized by XRPD, high temperature Mössbauer spectroscopy and high temperature Raman spectroscopy. The structural study by X-ray powder diffraction indicates that all intense diffraction peaks can be indexed according to a double perovskite structure with tetragonal I4/m symmetry, with $a = b = 5.6477(2)$, $c = 7.9874(3)$Å. The crystallographic formula can be written as $(Ba_{1.07}Sr_{0.93})_{4d}(Fe_{0.744}W_{0.256})_{2a}(Fe_{0.585}W_{0.415})_{2b}O_6$, Ba and Sr atoms occupy the 2d special positions in the A-site whereas the B-site contains a random distribution of Fe^{3+} and W^{6+} cations at alternating 2a and 2b crystallographic positions. The Mössbauer technique supported the existence of iron cations as Fe^{3+} only. The Mössbauer measurements show a transition from ferromagnetic to paramagnetic state at temperatures below 405 ± 10 K. The transition was gradual $\approx$20 K suggesting a temperature dependent ordering of the magnetic spins. The site occupancy obtained from Mössbauer data are in fair agreement with those obtained from Rietveld refinement and the parameters also support the existence of the magnetic order and are consistent with the presence of high-spin Fe^{3+} cations located in the octahedral B-site. The results of the study with high temperature Raman spectroscopy are indicative of minor structural changes, not revealed from Mössbauer spectroscopy. The senility of Raman shifts observed at increasing temperature may therefore be associated with relaxation phenomena in the structure at the transition. This structural transformation might be from the tetragonal symmetry at low temperatures to the cubic symmetry structure at high temperatures.

Acknowledgements

The authors are grateful to the Swedish Research Council and the Swedish International Development Co-operation Agency (Sida) for the financial grant (MENA) offered in support of this work.

References

[1] J. Navarro, C. Frontera, L. Balcells, B. Martinez, J. Fontcuberta, Phys. Rev. B 64 (2001) 92411.
[2] K.-I. Kobayashi, T. Kimura, H. Sawada, K. Terakura, Y. Tokura, Nature 395 (1998) 677.
[3] A. Maignan, B. Raveau, C. Martin, M. Hervieu, J. Solid State Chem. 144 (1999) 224.
[4] V. Pandey, V. Verma, R.P. Aloysius, G.L. Bhalla, V.P.S. Awana, H. Kishan, R.K. Kotnala, J. Magn. Magn. Mater. 321 (2009) 2239.
[5] K.-I. Kobayashi, T. Kimura, Y. Tomioka, H. Sawada, K. Terakura, Y. Tokura, Phys. Rev. B 59 (1999) 11159.
[6] T.H. Kim, M. Uehara, S.W. Cheong, S. Lee, Appl. Phys. Lett. 74 (1999) 1737.
[7] K.I. Koboyashi, T. Kimura, H. Sawada, K. Terakura, Y. Tokura, Nature 395 (1999) 677.
[8] W. Zhong, N.J. Tang, C.T. Au, Y.W. Du, J. Nanosci. Nanotechnol. 8 (2008) 1.
[9] G.Y. Liu, G.H. Rao, X.M. Feng, H.F. Yang, Z.W. Ouyang, W.F. Liu, J.K. Liang, J. Alloys Compd. 353 (2003) 42–47.
[10] M. El-Hagary, J. Alloys Compd. 502 (2010) 376–381.
[11] P.P. Hankare, M.R. Kadam, P.D. Kamble, S.D. Jadhav, U.B. Sankpal, R.P. Patil, V.B. Helavi, N.S. Gajbhiye, J. Alloys Compd. 489 (2010) 233–236.
[12] B.G. Kim, Y.S. Hor, S.W. Cheong, Appl. Phys. Lett. 77 (1996) 2041.
[13] A.H. Habib, A. Saleem, C.V. Tomy, D. Bahadur, J. Appl. Phys. 97 (10A) (2005) 906.
[14] B.J. Park, H. Han, J. Kim, C.S. Kim, B.W. Lee, J. Magn. Magn. Mater. 272–276 (2004) 1851.
[15] D.D. Sarma, E.V. Sampathkumaran, S. Ray, R. Nagarajan, S. Majumdar, A. Kumar, G Nalini, T.N. Guru Row, Solid State Commun. 114 (2000) 465.
[16] J. Rodriguez-Carvajal, Physica B 192 (1993) 55.
[17] P. Jernberg, T. Sundqvist, A Versatile Mössbauer Analysis Program, Uppsala University, Institute of Physics (UUIP-1090), 1983.
[18] A. Boultif, D. Louër, J. Appl. Cryst. 24 (1991) 987.
[19] S.A. Ivanov, S.-G. Eriksson, R. Tellgren, H. Rundlof, Mater. Res. Bull. 36 (2001) 2585.
[20] M.C. Viola, J.A. Alonso, J.C. Pedregosa, R.E. Carbonio, Eur. J. Inorg. Chem. (2005) 1559.
[21] S.A. Ivanov, P. Nordblad, S.-G. Eriksson, R. Tellgren, H. Rundlöf, Mater. Res. Bull. 42 (2007) 776.
[22] R.D. Shannon, Acta Cryst. A 32 (1976) 751.
[23] H.M. Rietveld, J. Appl. Cryst. 2 (1969) 65.
[24] A.M. Glazer, Acta Cryst. B 28 (1972) 3384.
[25] A.M. Glazer, Acta Cryst. A 31 (1975) 756.
[26] F. Menil, J. Phys. Chem. Solids 46 (7) (1985) 763.